Asteroids are young: global-scale reshaping and resurfacing by small-scale impacts

Sabina Raducan (sabina.raducan@unibe.ch)
University of Bern
Martin Jutzi
University of Bern

Article

Keywords: asteroids, double asteroid redirection test, sub-catastrophic impacts

Posted Date: September 30th, 2021

DOI: https://doi.org/10.21203/rs.3.rs-907971/v1

Asteroids are young: global-scale reshaping and resurfacing by small-scale impacts

S. D. Raducan*,[1] and M. Jutzi[1]

[1]Space Research and Planetary Sciences, Physikalisches Institut, University of Bern, Switzerland
(*E-mail: sabina.raducan@unibe.ch)

Abstract

The fraction of the asteroid population that survived since the Solar System formation has experienced numerous collisional, dynamical and thermal events, which have shaped their structures and orbital properties. Small asteroids are often considered to be rubble-pile objects, aggregates held together only by self-gravity or small cohesive forces (1; 2). The artificial impact experiment of JAXA's Hayabusa2 mission on the surface of asteroid Ryugu (3) created a surprisingly large crater (≈ 14 m). This unexpected result suggests that at least the near-surface of the asteroid is controlled to a large extent by its rather weak gravity rather than strength. Due to the inability to re-create these impact conditions in laboratory experiments, this observed regime of low-gravity, low-strength cratering remained largely unexplored so far. In addition, the very large times scales involved in the crater growth made it impossible to numerically simulate these impact processes up to now.

Here we use a novel approach to model the entire cratering process resulting from impacts on small, weak asteroids, which uses shock physics code calculations directly. We found that small impacts can significantly deform weak asteroids, causing global resurfacing at the same time. We also show that even very low asteroid cohesions can drastically influence the outcome of an impact and that the collisional life-time of the overall asteroid shapes is significantly lower than the traditionally used life-time based on catastrophic disruption events. Consequently, we predict that NASA's Double Asteroid Redirection Test (DART) impact on Dimorhpos (4; 5) will not lead to a cratering event, as originally anticipated (i.e., 6; 7). Rather, the impact is going to change the global morphology of the asteroid, if the surface cohesion is less than ≈ 10 Pa. Our results, together with the future observations by the ESA's Hera mission (8) will provide constraints regarding the evolution of the shapes and structures of small asteroids by sub-catastrophic impacts.

Measurements of asteroid collisional lifetimes and surface ages have an unknown accuracy due to their strong dependence on the target material properties (9; 10). Given the recent evidence of low-strength asteroids (e.g., 3; 11; 12), we studied small impact events on weak, low-gravity asteroids, and tracked the medium-long term evolution of the target, post-impact. The DART impact (4; 5) is an ideal study case because it takes place in the sub-catastrophic collision regime, a regime between cratering and catastrophic collisions (e.g., 13), that has been largely unexplored so far. With the help of the upcoming Hera mission, we will be able to assess the impact consequences and can make testable predictions.

To this end, we use Bern's parallel smoothed-particle hydrodynamics (SPH) impact code (14; 15; 16). We first explore the outcome of small, vertical impacts ($m \approx 500\,\mathrm{kg}$, $U = 6\,\mathrm{km/s}$), into 150 m spherical asteroids. The fate of the asteroid and of the ejected material was tracked for up to 2 hours after the impact. We use a new novel approach to perform end-to-end simulations of high velocity small body collisions, including the subsequent gravity-driven re-accumulation of fragments into final stable structures. In order to track the long evolution of the target, we used a modelling approach that allows for faster calculation times. This was achieved by applying a transition to a low-speed medium in the shock physics code. After the initial shock has passed, the late-stage evolution is governed by low-velocity granular flow that can be accurately described by a low bulk sound speed material, allowing for a larger numerical time-step (see Methods for details). The targets are modelled as porous basaltic aggregates ($\rho \approx 1600\,\mathrm{kg/m^3}$), with small amounts of cohesion (Y_0 = 0–50 Pa) and varying coefficient of internal friction (f = 0.4–1.0). The models used the Tillotson equation of state (17) and the target material response to shear deformation was described by a simple pressure-dependent strength model (18; 19). The initial target porosity was kept constant at 40% throughout this study, and was modelled using the $P-\alpha$ model (15), with a simple quadratic crush curve (see Methods).

We find that the mechanical strength properties of small asteroids are crucial for their physical evolution. A measure of strength is given by the material's ability to withstand different types of stress states. A granular material, for example, can still have a significant amount of shear strength originating from Van der Waals forces and the ability of the interlocking particles to move apart and slide over one another (20). Here we study the effects of the shear strength at zero pressure, which is often referred to as cohesion.

Our results show that even a small cohesion ($\lesssim 10\,\mathrm{Pa}$) can dramatically affect the outcome of an impact on a small body in terms of the post-impact target morphology and the production of low velocity ejecta. Two-dimensional slices through our 3D impact simulations of spherical asteroids, where we systematically varied the target cohesion and coefficient of internal friction, show the possible post-impact asteroid morphologies (Fig. 1). A quantitative measure of the shape deformation experienced by an asteroid as a result of an impact event is given in terms of the total strain experienced by the target material. The post-impact total strain is computed by integrating the second invariant of the strain-rate tensor for each SPH particle (see Methods).

For the cohesive ($Y_0 \gtrsim 1\,\mathrm{Pa}$) small asteroids simulated here, the target cohesion is the dominant force that stops the crater cavity from growing. Therefore, with decreasing target cohesion, more material is displaced and gets ejected above the escape speed of the target. With increasing coefficient of internal friction, more energy is needed to deform the target. Therefore, targets with higher f (and fixed cohesion) experience less total strain and have lower cratering efficiencies compared to targets with lower f. Regardless of our choice of target coefficient of internal friction, impacts into targets stronger than $Y_0 \approx 10\,\mathrm{Pa}$ create well defined bowl-shaped craters, while impacts into weaker targets create morphologies that are dissimilar to impact craters and cause the shape deformation of the target. For these scenarios ($Y_0 \lesssim 10\,\mathrm{Pa}$) the curvature of the target also plays a major role.

In our impact simulations, the mass-velocity distribution of ejecta that escapes the asteroid's gravitational field reproduces the power-law behaviour predicted by point-source approximation (21). The slope of the power-law is -3μ, where μ is commonly defined as the velocity scaling exponent (22). We find that while the target cohesion determines the total mass of ejecta, it does not influence the power-law slope of the ejecta mass-velocity distribution. For a fixed coefficient of internal friction ($f = 0.6$), we obtained $\mu = 0.38$. Increasing f causes a linear decrease in the power-law slope of the ejecta mass-velocity distribution, with $\mu = 0.39$ for $f = 0.4$ to $\mu = 0.36$ ($f = 1.0$). In Figure 2a we show the total mass of ejecta with velocities higher than $5\,\mathrm{cm/s}$ ($\approx v_{esc}$), from impacts into targets

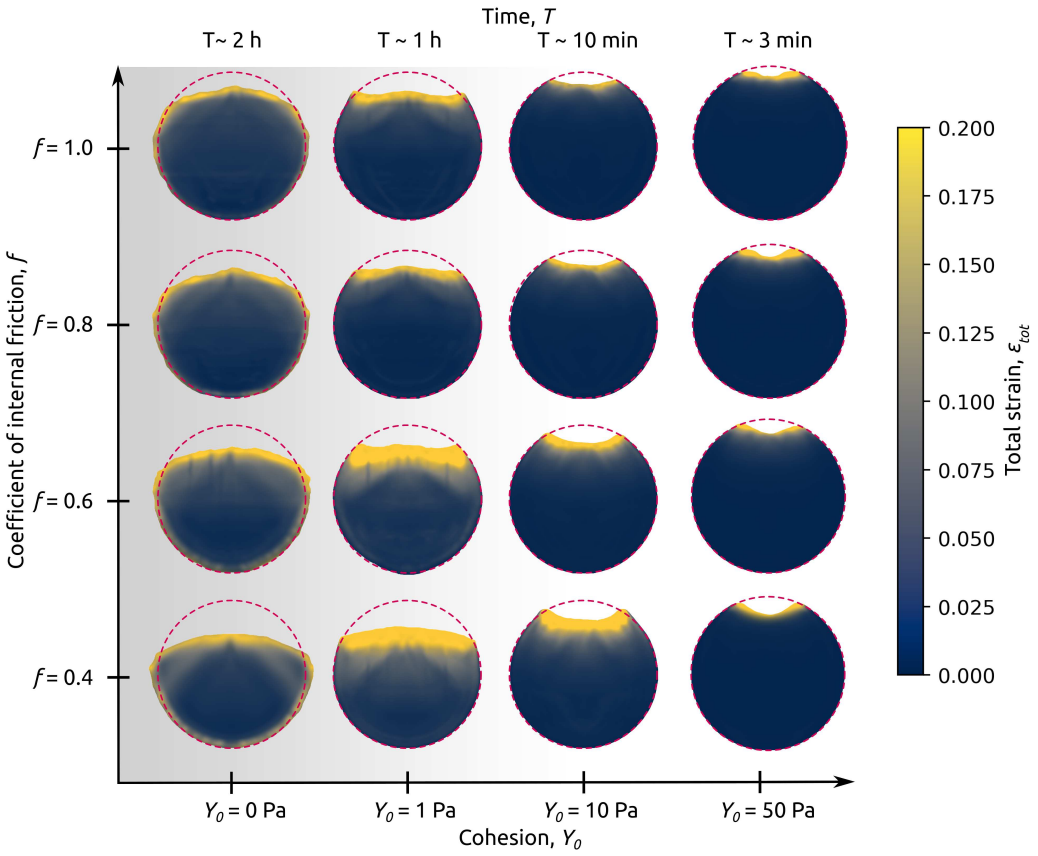

Figure 1: Two-dimensional slices showing possible asteroid morphologies after DART-like impacts on initially 150 m spherical bodies with varying cohesion (Y_0 = 0–50 Pa) and varying coefficient of internal friction (f = 0.4–1.0). Impacts into targets with Y_0 larger than $\approx$ 10 Pa create well defined craters, while impacts into targets with $Y_0 \lesssim 10$ Pa create the shape deformation of the asteroid. The total strain shows the amount of deformation experienced by the target. For a 150 m spherical asteroid ($\rho \approx 1600\,\mathrm{kg/m^3}$), the overburden pressure in the centre of the body is about 2 Pa. The background gradient shows the transition to the gravity dominated regime, where the target's overburden pressure at the cratering depth exceeds the cohesion.

with varying Y_0 and f. Similarly to the post-impact target shape, the target cohesion is the key parameter that influences the amount of mass thrown out from the growing crater cavity. While an impact on an asteroid with 50 Pa surface cohesion would produce $2 \times 10^4 \times m$ ejecta (where m is the impactor mass), an impact into a cohesionless target (Y_0 = 0 Pa) ejects up to 10 times more mass.

In the case of very low cohesion asteroids, only a relatively small fraction of the target material escapes the target. Instead there is significant material redistribution, leading to a change of the overall shape of the asteroid. We use the calculated total strain, together with the velocity change experienced by each SPH particle to distinguish between target material that escapes the asteroid's gravitational field, the material that gets deformed and is displaced on the target and material that does not experience large deformation. In Figure 2b we plot the amount of ejected target mass that is displaced on the asteroid surface, but does not escape the asteroid's gravitational field ($v < v_{esc}$).

During impacts into asteroids with cohesions larger than about 10 Pa, most of the material gets excavated from the crater with speeds larger than the escape velocity of the asteroid. The reason for this is that the ejected material is required to have a maximum speed exceeding that needed to overcome the cohesive strength of the target (23). On the other hand, in impact scenarios where the asteroid cohesion is smaller than about 10 Pa, the amount of mass displaced on the asteroid is much larger than the amount of mass that escapes the body's gravity (Fig. 2a, b). Therefore, on small, very weak asteroids we expect to find larger amounts of regolith than on small asteroids with moderate cohesion.

In a high velocity, vertical impact on an asteroid, the change in momentum of the asteroid, ΔP, can be amplified by the momenta of crater ejecta that exceeds the

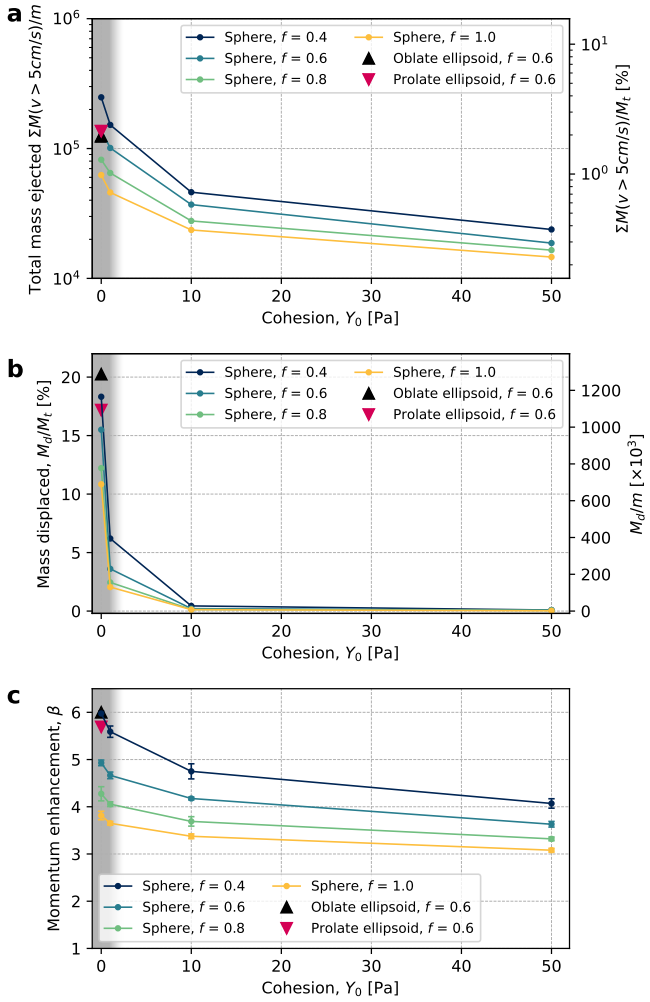

Figure 2: Asteroid mass ejected, displaced on the target and impact momentum enhancement. a) Total ejected mass at velocities above 5 cm/s ($\approx v_{esc}$), normalised by the projectile mass, m (left) and initial target mass, M_t (right). b) Total target mass below escape velocity that gets displaced on the target, normalised by the initial target mass, M_t (left) and projectile mass, m (right). c) Momentum transfer efficiency, β, for different target cohesions and different target coefficients of internal friction, f. The shaded area denotes the transition to the gravity-dominated cratering regime.

escape velocity (24). The efficiency of the momentum change is often expressed in terms of a quantity named the momentum enhancement factor, $\beta = \Delta P/mU$, where mU is the impactor momentum (7). Figure 2c shows β as a function of target cohesion for four different coefficients of internal friction.

Next, for a subset of the target parameters used in the spherical target scenarios ($Y_0 = 0\,\mathrm{Pa}$ and $f = 0.6$), we consider small impacts into oblate ($86 \times 86 \times 56\,\mathrm{m}$) and prolate ($100 \times 65 \times 65$ m) ellipsoid-shaped asteroids of similar masses. We find that the asteroid shape does not influence the amount of mass that is ejected above the escape speed of the target (Fig. 2a). However, the target geometry causes a clear amplification in the amount of displaced target mass and in the momentum transfer efficiency. Besides the difference in the gravitational acceleration on the body surface between the ellipsoidal and the spherical targets, the β amplification is also given by the target slope, which influences the ejection angle at launch position (β is calculated only from the vertical component of the of the escaping ejecta).

The average impact angle in the Main Belt is about 45 degrees (10). To generalise our findings, we compare SPH simulation results of vertical impacts to oblique impacts into equivalent targets (Fig 3), for a subset of impact conditions ($Y_0 = 0\,\mathrm{Pa}$ and $f = 0.6$). We find that for a spherical asteroid, the target mass experiencing a specific strain varies only by a few percent depending on the impact angle. We also find that for the very large cratering efficiencies seen here ($Y_0 \to 0\,\mathrm{Pa}$, see Supplementary for details), the ejecta momentum vector, which usually deviates from the surface normal for oblique impacts, here converges to the same direction as the surface normal. On the other hand, in the elliptical target scenarios, an impact angle different from vertical leads to less material deformation. Moreover, due to the non-symmetric target geometry, the location of the impact plays a major role in the post-impact target shape.

In the gravity dominated regime, the critical specific impact energy, Q^*_D, for the catastrophic disruption of an object of radius R can be approximated by $Q^*_D = a_g R^{3\mu_g} \times U^{2-3\mu_g}$ (25), where U is the impact velocity. In catastrophic disruptions, half of the original mass is dispersed. The material constant a_g and the velocity exponent μ_g for the targets used in this study are found by using a best fit algorithm through simulation results of impacts with different specific impact energies (see (26), Methods). For a $R = 75\,\mathrm{m}$ spherical asteroid, we find that the size and velocity dependence constants are $a_g = (1.0 \pm 0.2) \times 10^{-4}$ and $\mu_g = 0.39 \pm 0.01$ (Fig. 4).

As discussed above, our results show that only a relatively low specific impact energy is required to cause the shape deformation of the asteroid, rather than forming an impact crater. Using the same approach as for catastrophic disruption, we define $Q_{reshape}(20\%)$ as the energy required to displace 20% of the target mass. For $Q_{reshape}(20\%)$, we find $a_g = (1.8 \pm 0.5) \times 10^{-5}$ and $\mu_g = 0.38 \pm 0.02$. The μ_g values found here are comparable

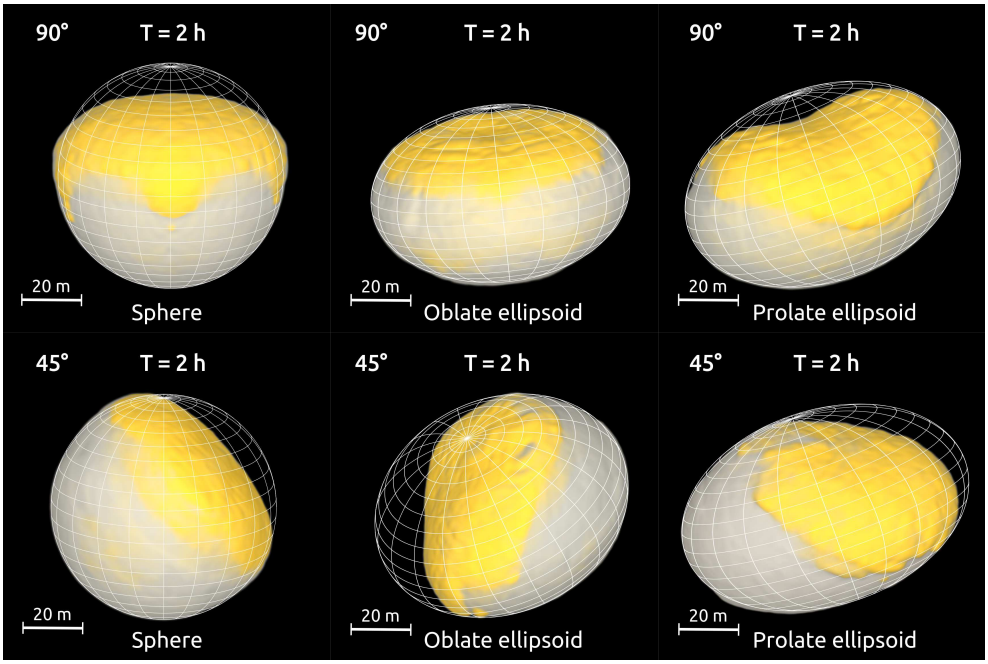

Figure 3: Asteroid target morphology after vertical (90°) and oblique (45°) impacts. Up to 20% of the target material gets displaced, causing excavation of material from the asteroid interior, global deformation and resurfacing. The colour denotes the deformed (strain>0.2) and displaced material. The white grid frame represents the initial geometry of the target. For better visualisation of the impact effects, some of the targets have been rotated.

with values generally assumed for typical porous materials (e.g., μ_g = 0.40–0.42 (26; 13); μ_g = 0.33–0.36 (27)). Moreover, the velocity exponent μ_g is similar to the μ value derived from ejecta scaling, which suggests that the point-source approximation holds for the small impacts studied here. Our simulation results of impacts into oblate and prolate ellipsoids (Fig. 4) indicate that the Q_D^* and $Q_{reshape}(20\%)$ are relatively insensitive to the target geometry. However, further dedicated studies are needed to investigate these impact scenarios in more detail.

We show that it is easier to cause global reshaping and resurfacing on small asteroids than previously believed. Because Q_D^* is much larger than $Q_{reshape}$, and given that small impacts are more common than larger ones, global reshaping and resurfacing events are expected to be up to five times more frequent than catastrophic disruptions (based on the approach used in (13)). Moreover, because reshaping impacts involve only very limited mass loss (few percent of the target mass), an asteroid may experience many reshaping events. Consequently, the collisional life-time of the overall asteroid shape is correspondingly smaller than its life-time before it gets catastrophically disrupted.

Our findings have strong implications for NASA's DART mission impact on Dimorphos (4; 5) and to ESA's Hera mission (8). The main goal of the DART mission is to alter Dimorphos's orbital period around the primary by an amount measurable from Earth (4). A successful deflection of Dimorphos will demonstrate the capabilities of a kinetic impact as an asteroid mitigation strategy. ESA's Hera mission (8) will arrive at Dimorphos several years after the DART impact and will perform a detailed char-

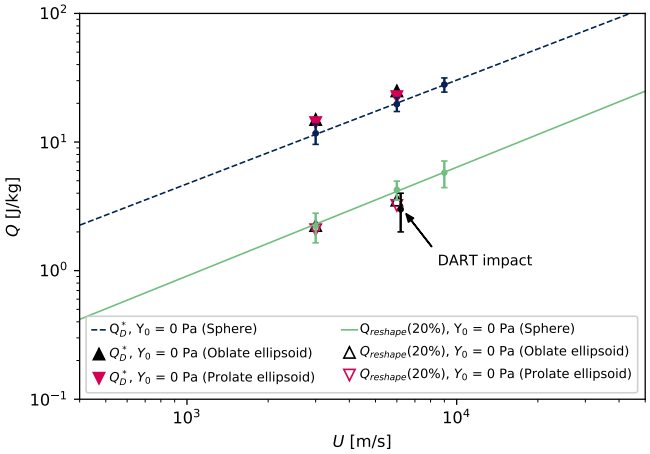

Figure 4: Critical specific impact energies for catastrophic disruptions, Q_D^*, and shape changing collisions, $Q_{reshape}(20\%)$, for cohesionelss ($Y_0 = 0Pa$) spherical and ellipsoidal targets. The DART specific impact energy is $Q_{DART} \approx 3 \pm 1$ J/kg.

acterisation of Dimorphos and of the DART impact outcome.

Measurements of the deflection efficiency and the DART impact crater size and morphology can be used to infer the target asteroid's mechanical properties (e.g., 28). The DART impact is expected to create a well defined crater on the surface of the asteroid (e.g., 6; 7). Our results show, however, that if Dimorphos's cohesion is very small ($Y_0 \lesssim 10\,\mathrm{Pa}$), then the DART impact will not create a crater, but instead will induce a global shape deformation of the asteroid. Moreover, in such impact scenarios the momentum enhancement factor, β, can be as high as six times the momentum of the impacting spacecraft, which is much larger than currently predicted values (e.g., 29; 30; 4). In addition to producing global shape deformation, the DART impact would probe not only the surface, but also the interior of the asteroid. These large shape deformations of Dimorphos will also lead to an additional change of the mutual orbit period, which is a critical parameter for calculating the kinetic impact deflection (31; 32).

Acknowledgements

This work has received funding from the European Union's Horizon 2020 research and innovation programme, NEOMAPP, under grant agreement No. 870377.

References

[1] Richardson, D. C., Leinhardt, Z. M., Melosh, H. J., Bottke, W. F., Jr. & Asphaug, E. Gravitational Aggregates: Evidence and Evolution. In *Asteroids III*, 501–515 (2002).

[2] Scheeres, D. J. *et al.* The dynamic geophysical environment of (101955) Bennu based on OSIRIS-REx measurements. *Nature Astronomy* **3**, 352–361 (2019).

[3] Arakawa, M. *et al.* An artificial impact on the asteroid (162173) ryugu formed a crater in the gravity-dominated regime. *Science* **368**, 67–71 (2020).

[4] Cheng, A. F. *et al.* AIDA DART asteroid deflection test: Planetary defense and science objectives. *Planetary and Space Science* **157**, 104–115 (2018).

[5] Rivkin, A. S. *et al.* The double asteroid redirection test (dart): Planetary defense investigations and requirements. *Planetary Science Journal* (2021).

[6] Stickle, A. M. *et al.* Modeling impact outcomes for the Double Asteroid Redirection Test (DART) mission. *Procedia Engineering* **204**, 116–123 (2017).

[7] Cheng, A. F. *et al.* Asteroid Impact & Deflection Assessment mission: Kinetic impactor. *Planetary and Space Science* **121**, 27–35 (2016).

[8] Michel, P. *et al.* European component of the AIDA mission to a binary asteroid: Characterization and interpretation of the impact of the DART mission. *Advances in Space Research* **62**, 2261–2272 (2018).

[9] Bottke, W. F. *et al.* The Collisional Evolution of the Main Asteroid Belt. In *Asteroids IV*, 701–724 (2015).

[10] Bottke, W. F., Love, S. G., Tytell, D. & Glotch, T. Interpreting the Elliptical Crater Populations on Mars, Venus, and the Moon. *Icarus* **145**, 108–121 (2000).

[11] Lauretta, D. S. *et al.* The unexpected surface of asteroid (101955) Bennu. *Nature* **568**, 55 (2019).

[12] Okada, T. *et al.* Highly porous nature of a primitive asteroid revealed by thermal imaging. *Nature* **579**, 518–522 (2020).

[13] Jutzi, M. The shape and structure of small asteroids as a result of sub-catastrophic collisions. *Planetary and Space Science* **177**, 104695 (2019).

[14] Benz, W. & Asphaug, E. Simulations of brittle solids using smooth particle hydrodynamics. *Computer Physics Communications* **87**, 253–265 (1995).

[15] Jutzi, M., Benz, W. & Michel, P. Numerical simulations of impacts involving porous bodies: I. Implementing sub-resolution porosity in a 3D SPH Hydrocode. *Icarus* **198**, 242–255 (2008).

[16] Jutzi, M. SPH calculations of asteroid disruptions: The role of pressure dependent failure models. *Planet. Space Sci* **107**, 3–9 (2015).

[17] Benz, W. & Asphaug, E. Catastrophic Disruptions Revisited. *Icarus* **142**, 5–20 (1999).

[18] Lundborg, N. The strength-size relation of granite. *International Journal of Rock Mechanics and Mining Sciences & Geomechanics Abstracts* **4**, 269–272 (1967).

[19] Collins, G. S., Melosh, H. J. & Ivanov, B. A. Modeling damage and deformation in impact simulations. *Meteoritics & Planetary Science* **39**, 217–231 (2004).

[20] Scheeres, D. J., Hartzell, C. M., Sanchez, P. & Swift, M. Scaling forces to asteroid surfaces: The role of cohesion. *Icarus* **210**, 968–984 (2010).

[21] Housen, K. R., Schmidt, R. M. & Holsapple, K. A. Crater ejecta scaling laws: Fundamental forms based on dimensional analysis. *Journal of Geophysical Research: Solid Earth* **88**, 2485–2499 (1983).

[22] Housen, K. R. & Holsapple, K. A. Ejecta from impact craters. *Icarus* **211**, 856–875 (2011).

[23] Raducan, S. D., Davison, T. M., Luther, R. & Collins, G. S. The role of asteroid strength, porosity and internal friction in impact momentum transfer. *Icarus* **329**, 282–295 (2019).

[24] Holsapple, K. A. & Housen, K. R. Momentum transfer in asteroid impacts. I. Theory and scaling. *Icarus* **221**, 875–887 (2012).

[25] Housen, K. R. & Holsapple, K. A. On the fragmentation of asteroids and planetary satellites. *Icarus* **84**, 226–253 (1990).

[26] Jutzi, M. & Benz, W. Formation of bi-lobed shapes by sub-catastrophic collisions: A late origin of comet 67P's structure. *Astronomy & Astrophysics* **597**, A62 (2017).

[27] Ballouz, R.-L. *et al.* Bennu's near-Earth lifetime of 1.75 million years inferred from craters on its boulders. *Nature* 1–5 (2020).

[28] Raducan, S. D., Davison, T. M. & Collins, G. S. The effects of asteroid layering on ejecta mass-velocity distribution and implications for impact momentum transfer. *Planetary and Space Science* 104756 (2020).

[29] Stickle, A. M. *et al.* Modeling Momentum Transfer from Kinetic Impacts: Implications for Redirecting Asteroids. *Procedia Engineering* **103**, 577–584 (2015).

[30] Bruck Syal, M., Michael Owen, J. & Miller, P. L. Deflection by kinetic impact: Sensitivity to asteroid properties. *Icarus* **269**, 50–61 (2016).

[31] Hirabayashi, M. *et al.* Constraints on the perturbed mutual motion in Didymos due to impact-induced deformation of its primary after the DART impact. *Monthly Notices of the Royal Astronomical Society* **472**, 1641–1648 (2017).

[32] Hirabayashi, M. *et al.* Assessing possible mutual orbit period change by shape deformation of Didymos after a kinetic impact in the NASA-led Double Asteroid Redirection Test. *Advances in Space Research* **63** (2019).

Supplementary Files

This is a list of supplementary files associated with this preprint. Click to download.

- Methods.pdf